Enhanced Terrestrial Carbon Export From East Antarctica During the Early Eocene

Gordon N. Inglis[1,2] ⓘ, Jaime L. Toney[3] ⓘ, Jiang Zhu[4] ⓘ, Christopher J. Poulsen[5] ⓘ, Ursula Röhl[6] ⓘ, Stewart S. R. Jamieson[7] ⓘ, Jörg Pross[8], Margot J. Cramwinckel[1] ⓘ, Srinath Krishnan[9,10], Mark Pagani[9,†] ⓘ, Peter K. Bijl[11], and James Bendle[12]

[1]School of Ocean and Earth Science, University of Southampton, Southampton, UK, [2]Organic Geochemistry Unit, School of Chemistry, University of Bristol, Bristol, UK, [3]School of Geographical and Earth Sciences, University of Glasgow, Glasgow, UK, [4]Climate and Global Dynamics Laboratory, National Center for Atmospheric Research, Boulder, CO, USA, [5]Department of Earth and Environmental Sciences, University of Michigan, Ann Arbor, MI, USA, [6]MARUM—Center for Marine Environmental Sciences, University of Bremen, Bremen, Germany, [7]Department of Geography, Durham University, Durham, UK, [8]Institute of Earth Sciences, Heidelberg University, Heidelberg, Germany, [9]Department of Geology and Geophysics, Yale University, New Haven, CT, USA, [10]CICERO Center for International Climate and Environmental Research, Oslo, Norway, [11]Department of Earth Sciences, Faculty of Geosciences, Utrecht University, Utrecht, The Netherlands, [12]School of Geography, Earth and Environmental Sciences, University of Birmingham, Birmingham, UK

Abstract Terrestrial organic carbon (TerrOC) acts as an important CO_2 sink when transported via rivers to the ocean and sequestered in coastal marine sediments. This mechanism might help to modulate atmospheric CO_2 levels over short- and long- timescales (10^3–10^6 years), but its importance during past warm climates remains unknown. Here we use terrestrial biomarkers preserved in coastal marine sediment samples from Wilkes Land, East Antarctica (∼67°S) to quantify TerrOC burial during the early Eocene (∼54.4–51.5 Ma). Terrestrial biomarker distributions indicate the delivery of plant-, soil-, and peat-derived organic carbon (OC) into the marine realm. Mass accumulation rates of plant- (long-chain *n*-alkane) and soil-derived (hopane) biomarkers dramatically increase between the earliest Eocene (∼54 Ma) and the early Eocene Climatic Optimum (EECO; ∼53 Ma). This coincides with increased OC mass accumulation rates and indicates enhanced TerrOC burial during the EECO. Leaf wax δ²H values indicate that the EECO was characterized by wetter conditions relative to the earliest Eocene, suggesting that hydroclimate exerts a first-order control on TerrOC export. Our results indicate that TerrOC burial in coastal marine sediments could have acted as an important negative feedback mechanism during the early Eocene, but also during other warm climate intervals.

Plain Language Summary Organic matter from the terrestrial biosphere can be transferred into rivers and eventually deposited in the ocean. This process helps to remove carbon dioxide from the atmosphere over long (>1,000 years) timescales. However, the importance of this process in warm climates is one of the most poorly understood aspects of the climate system. One way to test the behavior of the Earth in warmer-than-present climate states is to examine the geological record. Here we analyzed marine sediments deposited close to the Antarctic shoreline to quantify organic carbon burial during an ancient warm interval (the early Eocene, 56 to 48 million years ago). We analyzed biomolecules from plants and microbes to determine how much organic matter was derived from the terrestrial biosphere. We found evidence for increased terrestrial organic carbon burial in marine sediments during the early Eocene. This process could help to remove carbon dioxide from the atmosphere and is relevant to other episodes of climate change during Earth's history.

1. Introduction

Over long-timescales (10^4–10^6 years), the evolution of atmospheric carbon dioxide (CO_2) levels primarily reflects the balance between CO_2 sources (e.g., solid earth degassing, oxidation of rock-derived OC and sulphide minerals; Hilton et al., 2014; Plank & Manning, 2019; Torres et al., 2014) and CO_2 sinks (e.g., silicate weathering, organic carbon burial; Berner, 1990; Gaillardet et al., 1999; Galy et al., 2007). Between ∼20% and 50% of total OC burial in modern marine sediments is derived from the terrestrial biosphere (TerrOC; i.e., soils and vegetation; Hilton & West, 2020). Consequently, TerrOC burial in marine sediments may act as an important CO_2 sink over short-to long timescales (10^3–10^6 years; Hilton et al., 2015).

The erosion and subsequent burial of TerrOC in marine sediments is determined by a variety of climatic and tectonic controls (Eglinton et al., 2021). Steep river catchments are typically characterized by enhanced TerrOC export (e.g., Hilton, 2017; Kao et al., 2014). However, climate also exerts a key control on TerrOC export (Galy et al., 2015; Hilton, 2017) and there is a close link between mean annual run-off and TerrOC export in modern river systems (Hilton, 2017; Wang et al., 2020). Although TerrOC export and burial may help to modulate atmospheric CO_2 over geological timescales, the importance of this process in the past is unknown and the majority of work has been on modern erosive systems (e.g., Galy et al., 2015; Hilton, 2017; Wang et al., 2020).

The early Eocene Climatic Optimum (EECO; 53.3–49.1 Ma) is characterized by high temperatures (∼10°–16°C warmer than pre-industrial; Inglis et al., 2020), an intensified hydrological cycle (Carmichael et al., 2016), and lacked continental-scale ice sheets (Francis & Poole, 2002). As such, it can serve as a natural laboratory to understand how TerrOC export and burial operates when it is significantly warmer and wetter than present. Here we use samples recovered from the East Antarctic margin (Integrated Ocean Drilling Program (IODP) Leg 318; IODP Site U1356; ∼67°S paleolatitude; Escutia, Brinkhuis, Klaus, Bendle, et al., 2011) to determine the amount of TerrOC transported along the land-sea continuum during the earliest Eocene (54.3–51.5 Ma), including one of the three DeepMIP intervals (i.e., the Early Eocene Climatic Optimum; 53.3–49.1 Ma; Hollis et al., 2019). A combination of bulk and molecular proxies are used to fingerprint the type of OC in the East Antarctic margin. We then apply a mixing model approach to quantify TerrOC burial along the East Antarctic margin. We also develop new leaf wax δ^2H records and compare these alongside isotope-enabled modeling simulations to determine the relationship between the hydrological cycle and TerrOC export during the early Eocene.

2. Methods and Materials

2.1. Site Description

Site U1356 (modern coordinates: 63°18.6138′ S, 135°59.9376′ E) is located ∼300 km off Wilkes Land, Antarctica, at the transition between the continental rise and the abyssal plain. Current water depth is 3,992 m (Escutia, Brinkhuis, & Klaus, 2011a; Figure 1). Samples were obtained from lithological Unit XI (∼948–1,000 mbsf) that consists of bioturbated hemipelagic early Eocene claystones. Occasional laminated siltstone and sandstone interbeds indicate sporadic gravity flows or bottom current activity reaching the site (Escutia, Brinkhuis, & Klaus, 2011). Lithological Unit XI is dated as early Eocene based upon a combination of published dinoflagellate cyst (dinocyst) biostratigraphy and magnetostratigraphy (Bijl et al., 2013; Tauxe et al., 2012).

2.2. Bulk Isotope Geochemistry

Total organic carbon (TOC) measurements were carried out at MARUM, University of Bremen. Approximately 10 cm^3 of sediment ($n = 360$) was freeze-dried and ground to a fine powder using an agate mortar. Total carbon (TC), total organic carbon (TOC), and total sulphur (TS) were measured using a LECO CS-200 Carbon-Sulphur analyzer. Approximately 65 mg of the homogenized sample was weighed in a ceramic cup and burnt in an induction furnace. The resultant CO_2 and SO_2 were then measured with a nondispersive infrared detector to provide a measure of the sedimentary TC and TS content. To determine the TOC content, sediments (∼65 mg) were decalcified using 12.5% hydrochloric acid (HCl) to remove carbonate species, followed by a subsequent rinse of the residue with de-ionized water. Samples were subsequently analyzed as described above. Total inorganic carbon (TIC) was determined by subtracting TOC from TC. All data are reported in weight percent (wt. %) dry sample.

Bulk carbon isotope analyses of the OC fraction ($\delta^{13}C_{org}$) were carried out at MARUM, University of Bremen at 2 cm resolution throughout Cores 318-U1356A-103R to −106R ($n = 368$). The bulk samples were decalcified with 1 N HCl solution, followed by a subsequent rinse of the residue with de-ionized water. The sample was then combusted using the oven of an HERAEUS CHN-Analyzer. The $\delta^{13}C$ value was subsequently measured with a Finnigan MAT Delta E Mass-spectrometer. Measurements were calibrated using a house standard (milled and decalcified organic-rich surface sediment from the German Wadden Sea), itself calibrated to international standards. Repeatability of the house standard is typically ±0.15‰.
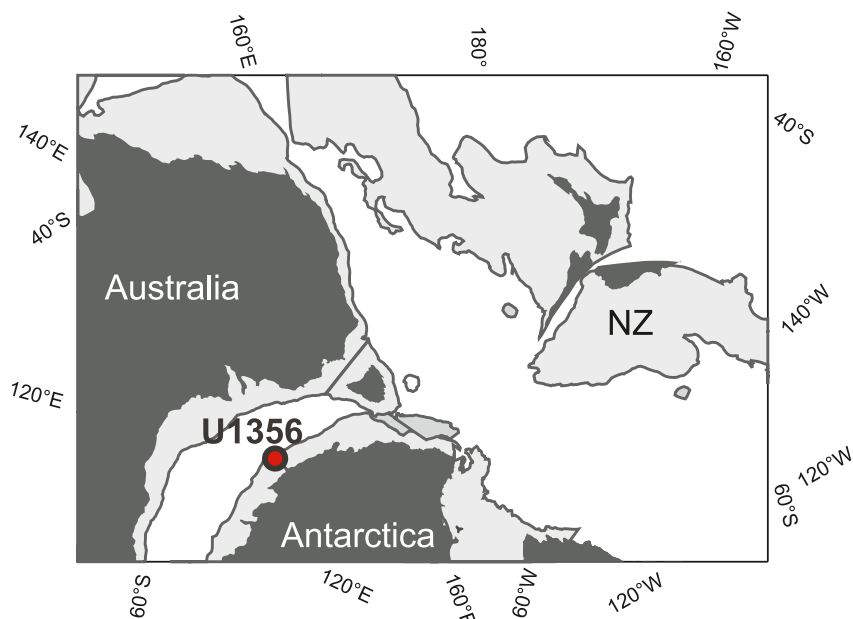
Figure 1. Continental configurations of the Australian sector of the Southern Ocean during the early Eocene (subchron C24n; 53.8 Ma). Map shows the position of the study site (U1356). Dark gray areas reflect present day shorelines, and light gray areas are submerged continental blocks above 3,000 m water depth. Modified from Bijl et al. (2013).

2.3. Organic Geochemistry

A total of 118 sediment samples (~10–15 g dry mass) from IODP Site 1356 (948.96–998.1 mbsf) were freeze-dried and extracted using Accelerated Solvent Extraction with dichloromethane (DCM) and methanol (MeOH; 9:1, v/v, respectively) as the organic solvent. An internal standard (5α-andostrane) with a known concentration was added to each sample prior to extraction. Excess solvent was removed using rotary evaporation under vacuum. The total lipid extract (TLE) was separated into "apolar," "ketone," "ethyl acetate" (EtOAc), and "polar" fractions over an activated alumina (Al_2O_3) column using hexane:DCM (9:1, v/v; N1), hexane:DCM (1:1, v/v; N2), EtOAc:DCM (1:1 v/v; N3), and DCM:MeOH (1:1, v/v; N4), respectively. Al_2O_3 was activated by oven-drying for at least 4 hr at 150°C.

For a subset of earliest Eocene samples ($n = 11$), we performed urea adduction on the N1 fractions to separate cyclic (i.e., non-adduct) and aliphatic (i.e., adduct) hydrocarbons. To achieve this, 200µl of hexane, acetone and urea (10% in MeOH) were added to the saturated hydrocarbon fraction. The sample was frozen for ca. 60 minutes until urea crystals formed. Solvent was then removed under a stream of N_2 and extracted (x5) with ca. 1ml of n-hexane (non-adduct fraction). The urea crystals were then dissolved in 500 µl of MeOH and 500 µl of water and the adduct fraction was extracted (x5) with ca. 1ml of n-hexane. The adduction procedure was repeated on the adduct fraction once more to ensure all non-adduct material was removed (Inglis et al., 2019).

2.3.1. GC and GC-MS Analysis

N1 fractions were redissolved in hexane and analyzed using a gas chromatograph (GC; Shimadzu 2010) with a flame ionization detector (FID) and hydrogen as carrier gas at constant pressure (190 kPa). Separation of the different compounds was achieved using the following column: length: 60 m, diameter: 0.25 mm, film thickness: 0.25 µm, coating: 100% dimethyl-polysiloxane. The gas chromatograph temperature program increased from 50° to 120°C at 30°C min^{-1}, then 120°–310°C at 5°C min^{-1}, with a final isothermal time of 20 min at 300°C. Compound identification was confirmed by GC-MS (Shimadzu QP2010-Plus Mass Spectrometer (MS) interfaced with a Shimadzu 2010 GC) using the same column described above. Compounds were identified using retention times and mass spectra. The abundance of n-alkanes and hopanes are normalised to TOC. An in-house external standard comprised of 20 n-alkanes (ranging from C_{16} to C_{37}) was run every 10 samples to monitor analytical performance.

2.3.2. GC-C-IRMS Analysis

Compound specific hydrogen isotopic compositions were determined for a subset of samples from the earliest Eocene ($n = 11$) and EECO ($n = 5$). We analyzed long-chain (C_{27}, C_{29}) n-alkanes via gas chromatography-combustion-isotope ratio mass spectrometry (GC-C-IRMS) using a ThermoFisher Trace GC Ultra coupled to a ThermoFisher Scientific Delta V Isotope Ratio MS. The GC column used was a 30 m × 0.25 mm i.d. fused silica column with ZB1 stationary phase. The H_3 factor was measured daily allowing isotope values to be corrected for protonation reactions occurring within the ion source of the mass spectrometer (Sessions et al., 1999). The H_3 factor was typically below 5 ppm mV^{-1} and had a rate of change of less than 0.1 day^{-1}. The GC program was as follows: starting temperature 70°C, rising at 10°C/min to 300°C, at which point the oven temperature was held stable for 8 min, giving a total analysis-time of 32 min. Triplicate runs of each sample were performed. The average standard error of the mean (SEM) value for a triplicate measurement was typically 2–7‰. Each individual sample was co-injected with sacrificial compounds consisting of n-pentadecane and ethyl caprylate to condition the reactor. Measured isotope values were normalised by comparing the instrument's response to a suite of n-alkanes with a known isotopic composition (B5 mix; supplied by A. Schimmelmann, Indiana University, USA) injected before and after each triplicate of sample runs. The root mean square error determined by replicate measurements of the standard across the course of analyses was between 4 and 7‰. Normalised results are reported in standard per mil (‰) notation as δ^2H values relative to Vienna Standard Mean Ocean Water (VSMOW) and calculated against calibrated H_2 gas, introduced directly into the ion source.

2.4. Lipid Biomarker Proxies

We use biomarkers ratios to assess the source and maturity of organic matter. The average chain length (ACL) expresses the average number of carbon atoms for the long-chain odd-carbon numbered n-alkanes (Pancost & Boot, 2004). The ACL is defined for n-alkanes using the following equation (Eglinton & Hamilton, 1967):

$$ACL = (25 \times C_{25}) + (27 \times C_{27}) + (29 \times C_{29}) + (31 \times C_{31}) + (33 \times C_{33})/(25 + 27 + 29 + 31 + 33) \tag{1}$$

The carbon preference index (CPI) reflects the dominance of odd-carbon-numbered relative to even-carbon-numbered n-alkane homologs (Bray & Evans, 1961). Modern sediments exhibit high CPI values (>3–30; Diefendorf & Freimuth, 2017). This value decreases over time due to diagenesis, approaching values of unity (=1) in mature rocks and oils. The CPI is defined using the following equation (Bray & Evans, 1961):

$$CPI = 0.5 \times ((C_{25} + C_{27} + C_{29} + C_{31}/C_{26} + C_{28} + C_{30} + C_{32}) + (C_{27} + C_{29} + C_{31} + C_{33}/$$
$$C_{26} + C_{28} + C_{30} + C_{32})) \tag{2}$$

The hopane $\beta\beta/(\alpha\beta+\beta\beta)$ ratio is used to evaluate changes in sediment maturity. Modern sediments exhibit high hopane $\beta\beta/(\alpha\beta+\beta\beta)$ ratios (up to 1) whereas thermally mature rocks and oils are characterized by lower hopane $\beta\beta/(\alpha\beta+\beta\beta)$ ratios (Mackenzie et al., 1980), although there can be exceptions (e.g., acidic peats; Inglis et al., 2018). With increasing maturation, C_{31} to C_{35} hopanes also undergo isomerization at the C-22 position. An increase in 22S/(22R + 22S) values is characteristic of increasing thermal maturation (Mackenzie et al., 1980).

2.5. Mass Accumulation Rates

Biomarker mass accumulation rates (MARs; in ng/cm^2/kyr^{-1}) are calculated using linear sedimentation rate (LSR; cm/kyr), dry bulk density (ρ; g/cm^3; Dadey et al., 1992) and biomarker abundance (ng/g dry sediment):

$$MAR = LSR * \rho * \text{ biomarker abundance} \tag{3}$$

Linear sedimentation rates (LSRs) are calculated between the age tie-points. To avoid age inversions (i.e., within Core 105R-1) we constructed LSRs based on a selection of tie points rather than incorporate all bio- and magnetostratigraphic datums in the age model (see Supporting Information S1).

2.6. Continental Shelf Area Calculations

We calculate continental shelf area using the Eocene-Oligocene (ca. 34 Ma) paleotopography published elsewhere (Hochmuth, Gohl, et al., 2020, Hochmuth, Paxman, et al., 2020; Paxman et al., 2019). The same calculations are also conducted using Bedmap2 (Fretwell et al., 2013) for the present day. Continental shelf area for the
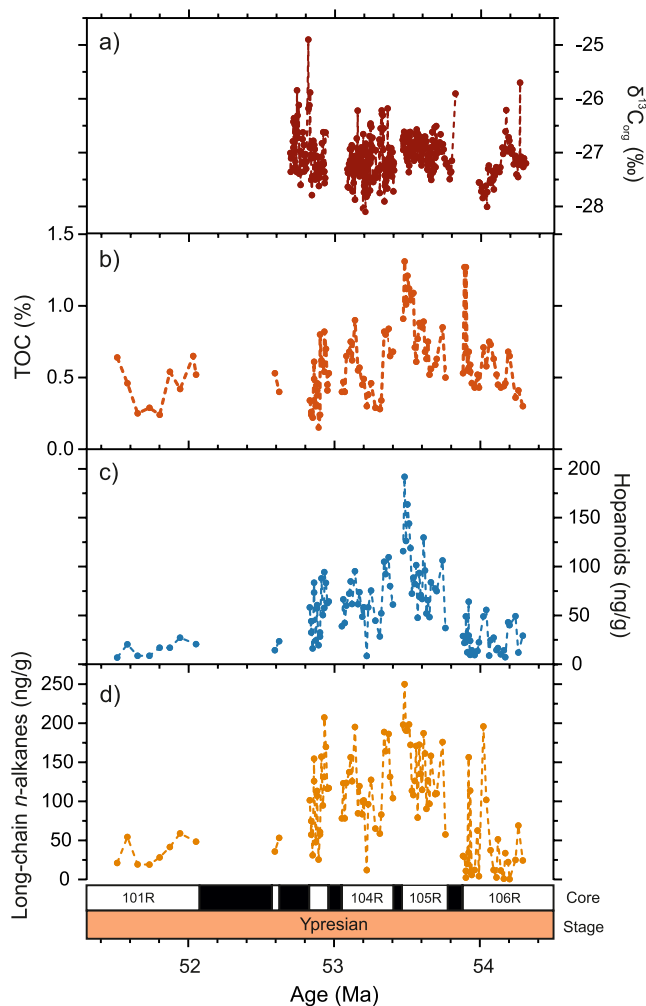
Figure 2. Organic carbon burial along the East Antarctic margin during the early Eocene. (a) $\delta^{13}C_{org}$ (‰), (b) total organic carbon (TOC; wt. %), (c) bacterial-derived hopanoids (ng/g), (d) plant-derived long-chain *n*-alkanes (ng/g). Black segments indicate intervals of no core recovery.

Eocene is defined as being from the 0 m contour (e.g., shore of an ice free Antarctica) to the −1000 m bathymetric contour (Figure S1 in Supporting Information S1). We calculate continental shelf area for the region directly adjacent to Wilkes basin and for the whole Antarctic continent in order to understand potential (Terr)OC sequestration.

2.7. Modeling Simulations

δ^2H_{wax} is usually employed as a proxy for the isotopic composition of precipitation (δ^2H_w). However, this integrates a combination of climatic changes including temperature, rainfall amount and characteristics, and atmospheric vapor transport. Here we use modeled δ^2H_w obtained via the isotope-enabled Community Earth System Model version 1.2 (iCESM1.2; Zhu et al., 2019, 2020) to compare with our proxy reconstructions and to aide climatic interpretation of δ^2H_w (Lee et al., 2007; Schmidt et al., 2007). The iCESM1.2 simulations were performed following protocols of the Deep-time Model Intercomparison Project (Lunt et al., 2017, 2021) with the Eocene paleogeography and vegetation (56.0–47.8 Ma; Herold et al., 2014) and atmospheric CO_2 levels of ×1, ×3, ×6, and ×9 the preindustrial value (284.7 ppmv). The different atmospheric CO_2 levels span the range of proxy-derived CO_2 estimates for the early Eocene (Anagnostou et al., 2020). We also carried out a single pre-industrial simulation to isolate the non-CO_2 component on δ^2H_w (i.e., changes due to paleogeography, vegetation, aerosols, and lack of continental ice sheets). All simulations were run at a horizontal resolution of 1.9° × 2.5° (latitude × longitude) for the atmosphere and land, and a nominal 1° for the ocean and sea ice. Of particular relevance to this study is the capability of iCESM1.2 to simulate the transport and transformation of oxygen and hydrogen isotope ratios ($\delta^{18}O$ and δ^2H) in the climate system (Brady et al., 2019). Seawater $\delta^{18}O$ and δ^2H in the simulations were initialized from constant values of −1.0‰ and −8.0‰, respectively, to account for the absence of ice sheets in a hothouse climate (Hollis et al., 2019). The simulations were run for more than 2000 years with the surface climate and water isotopes close to equilibration. The simulations capture the magnitude of Eocene global warmth, the reduction in the meridional gradient of sea-surface temperature, and the overall values and distribution of marine planktic foraminifera $\delta^{18}O$. Readers are referred to Zhu et al. (2019, 2020) for details of the experimental setup, equilibration state, and assessment of the simulation results.

3. Results

3.1. Bulk Geochemistry

Total organic carbon (TOC) content ranges between 0.1% and 1.5% (Figure 2). There is a gradual increase in TOC values between 54.4 and 53.5 Ma (Core 106R to 105R) followed by a gradual decrease thereafter (53.5–52.7 Ma, Core 104R to 101R). Bulk $\delta^{13}C_{org}$ values range between −25.7 and −28.1‰ (Figure 2). The early Eocene record from Site U1356 exhibits several $\delta^{13}C_{org}$ variations. These $\delta^{13}C_{org}$ cycles and excursions have maximum values of up to −26‰ (in one case −25‰). The average $\delta^{13}C_{org}$ values of −26 to −28 ‰ are typical for terrestrial organic matter (Hayes, 1993), although this value may be different in the Eocene (Sluijs & Dickens, 2012). The cyclicity in the $\delta^{13}C_{org}$ record is relatively pronounced in the lower part of the studied section (Cores U1356-105R and −106R; Figure 2), where TOC values are high enough (0.5–1.2 wt. %) to provide robust data. In the upper part of the early Eocene section (e.g., Cores 103R and −104R), TOC contents are often lower than 0.5 wt. % and yield a lower fidelity $\delta^{13}C_{org}$ signal.
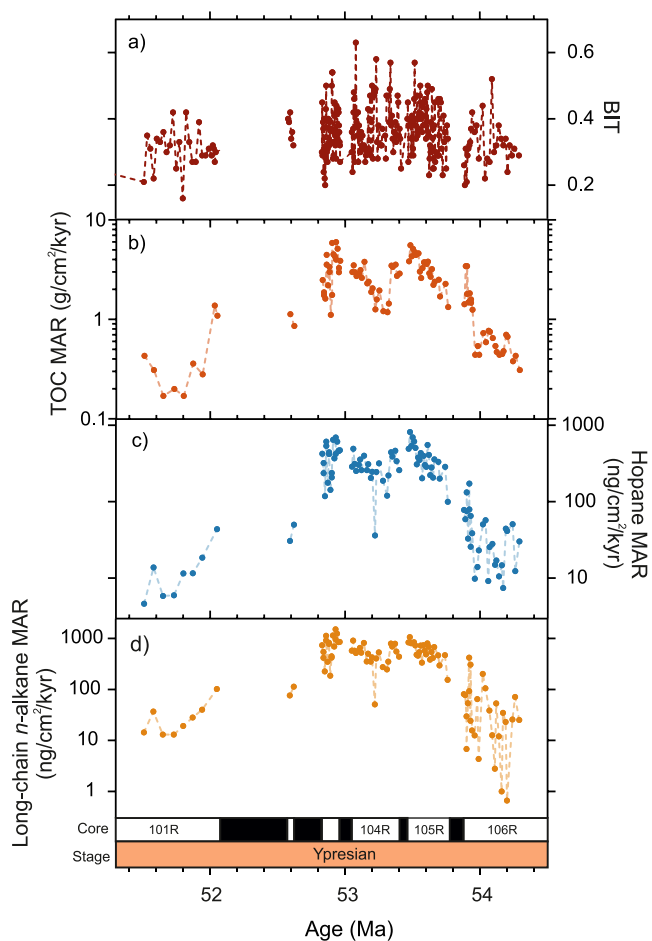
Figure 3. Enhanced terrestrial organic carbon burial along the East Antarctic margin during the Eocene. (a) branched-versus-isoprenoidal tetraether (BIT) index (Bijl et al., 2013), (b) total organic carbon (TOC; g/cm²/kyr⁻¹) mass accumulation rate (MAR), (c) hopanoid MAR (ng/cm²/kyr⁻¹), (d) long-chain n-alkane MAR (ng/cm²/kyr⁻¹). Note that (a–c) are on a logarithmic scale. Black segments indicate intervals of no core recovery.

3.2. Biomarker Distributions and Mass Accumulation Rates

The N1 fraction contains a range of n-alkanes (C_{17} to C_{33}) and is dominated by long-chain homologs (C_{27} to C_{33}). The abundance of long-chain n-alkanes ranges between ~1 and 250 ng/g (average: 92 ng/g; Figure 2d). Long-chain n-alkane (plant-derived OC; Figure 3d) mass accumulation rates (MARs; in ng/cm²/kyr⁻¹) increase by two orders-of-magnitude between the earliest Eocene (~54 Ma) and the onset of the EECO (~53 Ma; Figure 3). CPI values (average: 2.8; Figure 4a) indicate that long-chain n-alkanes have retained a biological odd-over-even predominance. In combination with high ACL values (~27–30; Supplementary Information), this confirms they are derived from terrestrial higher plants (Diefendorf & Freimuth, 2017).

The apolar fraction also contains a range of bacterial-derived hopanes (C_{27} to C_{32}) and hopenes (C_{27} to C_{30}). The abundance of hopanes ranges from ~1 to 191 ng/g (average: 54 ng/g) and exhibits a significant linear correlation with long-chain n-alkane abundance ($r^2 = 0.81$, $p < 0.001$; Figure S2 in Supporting Information S1). Hopane (soil- and peat-derived OC; Figure 3d) mass accumulation rates (MARs; in ng/cm²/kyr⁻¹) increase by two orders-of-magnitude between the earliest Eocene (~54 Ma) and the onset of the EECO (~53 Ma; Figure 3). The dominant hopanes are (22R)-17β,21β (H)-hopane (C_{30}), (22R)-17α,21β (H)-homohopane (C_{31}) and (22R)-17β,21β (H)-homohopane (C_{31}). The C_{31} hopane ββ/(αβ+ββ) isomerization ratio ranges between 0.31 and 0.82 (average: 0.65; Figure 4b). The earliest Eocene (54.3–53.7 Ma) samples (Core 106R) are characterized by the lowest C_{31} ββ/ (αβ+ββ) indices (0.4–0.6). C_{31} ββ/(αβ+ββ) indices increase during the early Eocene (~53.7 Ma) and remain higher (~0.5–0.8) thereafter (Cores 105R to 101R) with the exception of two relatively low values between 949 and 950 mbsf (Core 101R; Figure 4b). C_{30} ββ/(αβ+ββ) indices were stable and high (~0.7–0.8). C_{31} hopane 22S/(22S + 22R) ratios were stable and low (<0.1).

Our analyses are combined with previously published Branched-versus-Isoprenoid Tetraether (BIT) values (Bijl et al., 2013). BIT values range between 0.16 and 0.62 (average: 0.35) and exhibit higher values (>0.4–0.5) during the EECO (Core 105R to 102R; Supplementary Information) compared to the earliest Eocene (Core 106R).

3.3. Long-Chain n-alkane δ²H Values

Long-chain n-alkane δ²H (δ²H$_{wax}$) values were determined for a subset of samples ($n = 15$) deposited during the earliest Eocene (54.3–53.9 Ma) and across the EECO (53.3–49.1 Ma). C_{27} n-alkane δ²H values average −190‰ ($n = 15$, standard error of the mean [SEM]: ±4.0‰) with a range from −140 to −222‰ (Figure 5a). C_{29} n-alkane δ²H values average −194‰ ($n = 15$, SEM: ±2.9‰) with a range from −158 to −224‰ (Figure 5a). Both the C_{27} and C_{29} n-alkanes co-vary and exhibit a positive linear relationship ($r^2 = 0.78$, $p < 0.001$), indicating that they are derived from a similar source (i.e., higher plants; Figure S3 in Supporting Information S1).

4. Discussion

4.1. Enhanced TerrOC Burial on the East Antarctic Margin During the EECO

The export of terrestrial OC along the terrestrial-aquatic continuum can be evaluated by analyzing the distribution of lipid biomarkers within the Wilkes Land sediment samples. The hydrocarbon distribution is dominated by long-chain n-alkanes with an odd-over-even predominance. High CPI values (~3; Figure 4a) together with the dominance of long-chain n-alkanes (relative to shorter-chain homologs) confirms that they are derived from the epicuticular wax of terrestrial higher plants (Eglinton & Hamilton, 1967). The hydrocarbon assemblage also
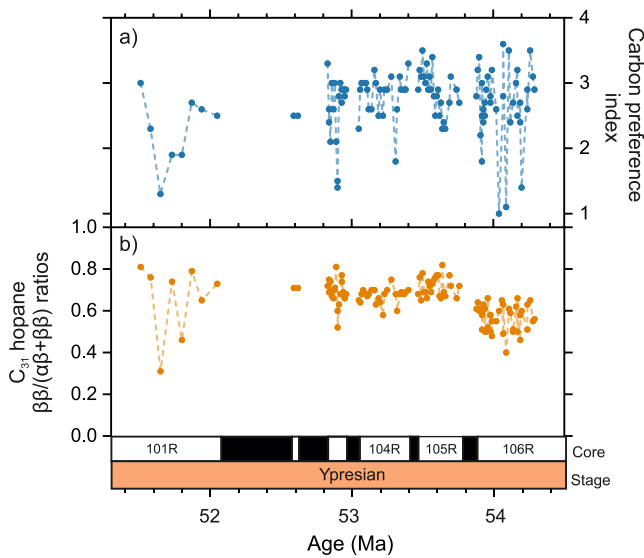
Figure 4. Lipid biomarker thermal maturity ratios in early Eocene-aged Wilkes Land sediments. (a) long-chain *n*-alkane carbon preference index (CPI), (b) C_{31} hopane $\beta\beta/(\alpha\beta+\beta\beta)$ indices. Black segments indicate intervals of no core recovery.
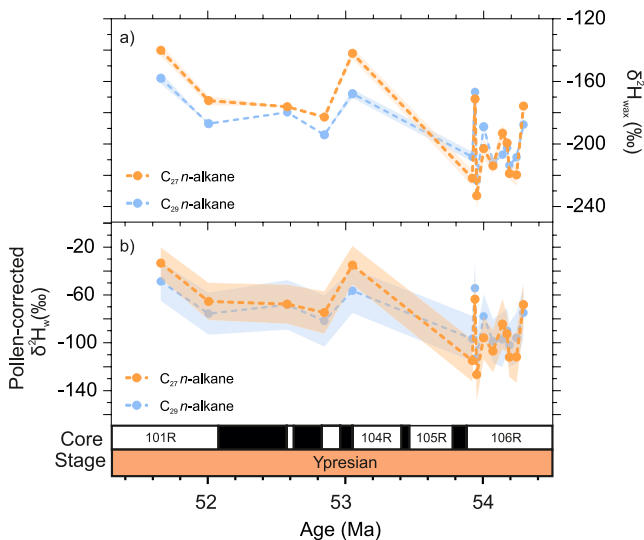

Figure 5. Enhanced poleward moisture transport to the East Antarctic margin during the early Eocene. (a) δ^2H_{wax} estimates inferred from the C_{27} *n*-alkane (orange) and C_{29} *n*-alkane (blue). Error bars represent $\pm 1\sigma_{\bar{x}}$ (following Polissar & D'Andrea, 2014). (b) pollen-corrected proxy-derived δ^2H_w estimates inferred from the C_{27} *n*-alkane (orange) and C_{29} *n*-alkane (blue). Error bars indicate $\pm 1\sigma$ propagated errors of the analytical error and the fractionation uncertainty (following Feakins, 2013). Here we use the standard deviation from modern plant type groups (i.e., C_3 angiosperms, C_3 gymnosperms, ferns; Sachse et al., 2012) to calculate the fractionation uncertainty (see Open Research).

contains abundant bacterial-derived hopane biomarkers. Hopanes can be produced in terrestrial and marine environments by a range of bacteria (Talbot & Farrimond, 2007). However, the positive linear relationship between long-chain *n*-alkanes (terrestrial higher plants) and hopanes ($r^2 = 0.81$; $p < 0.001$; Figure S2 in Supporting Information S1) indicates that here, both are sourced from the terrestrial biosphere.

Long-chain *n*-alkane (plant-derived OC; Figure 4d) and hopane (soil-derived OC; Figure 4c) mass accumulation rates (MARs; in ng/cm²/kyr⁻¹) increase by two orders-of-magnitude between the earliest Eocene (∼54 Ma) and the onset of the EECO (∼53 Ma). This significant increase indicates enhanced burial of plant- and soil OC during the early Eocene, with highest accumulation rates during the EECO. Note that we performed the same calculations assuming a constant LSR (1.82 cm/year, i.e., the average LSR rate) and find similar MARs during the EECO (∼53 Ma; Figures S4–S5 in Supporting Information S1). Delivery of TerrOC into the marine realm is consistent with the high abundance of terrestrial palynomorphs (i.e., pollen and spores; (Contreras et al., 2013; Pross et al., 2012) and other terrestrial biomarkers (including high BIT indices; Bijl et al., 2013; Pross et al., 2012; Figure 3a) in the same sediments. These findings are analogous to those observed in modern (high-latitude) environments, where large river systems in northern Eurasian and North American (Guo et al., 2004; Hilton et al., 2015; Semiletov et al., 2011; Sparkes et al., 2015) are capable of transporting large quantities of TerrOC from soils into the marine realm.

The earliest Eocene sediments also contain an unusually high abundance of the "thermally mature" C_{31} 17α,21β(H) hopane stereoisomer and exhibit relatively low C_{31} hopane $\beta\beta/(\alpha\beta+\beta\beta)$ ratios (0.4–0.7; Figure 4b). This implies delivery of biospheric (i.e., thermally immature) and petrogenic OC (i.e., thermally mature) into the marine realm. Input of petrogenic OC should be associated with the delivery of other thermally mature hopanes (e.g., C_{30} αβ hopanes). However, C_{30} hopane $\beta\beta/(\alpha\beta+\beta\beta)$ values remain relatively high (>0.7), implying minimal petrogenic OC input. Modern acidic bogs can be dominated by the "thermally mature" C_{31} 17α,21β(H) isomer (Inglis et al., 2018), but typically lack other thermally mature hopanes (e.g., C_{30} αβ hopanes; Inglis et al., 2018). We therefore argue that the occurrence of the "thermally mature" C_{31} 17α,21β(H) stereoisomer within an otherwise immature hopane assemblage represents input of acidic peat into the marine realm. The occurrence of the "thermally mature" C_{31} 17α,21β(H) stereoisomer within recent coastal marine sediments has also been interpreted to reflect input of peat from the surrounding catchment (Smittenberg et al., 2004). This hypothesis helps explain why C_{30} and C_{29} hopane $\beta\beta/(\alpha\beta+\beta\beta)$ values remain relatively high throughout (>0.7). It is also consistent with the lack of other thermally mature biomarkers (e.g., αβ 22S-hopanoid isomers, bisnorhopanes, benzohopanes, triaromatic steroids) and relatively high CPI values (>3; Figure 4a).

Input of acidic peat into the marine realm is consistent with the occurrence of *Stereisporites* spores in the Site U1356 sediments (Pross et al., 2012; Figure S6 in Supporting Information S1) that can be attributed to the Sphagnaceae family, which today only comprises the genus *Sphagnum* (commonly known as peat moss). Despite the low abundances registered, the occurrence of *Stereisporites* spores in the Site U1356 sediments appears noteworthy for various reasons. First, *Stereisporites* spores are relatively rare or absent in early Cenozoic sediments (see Inglis et al., 2015 and ref. therein). Second, spores

are generally strongly underrepresented in sporomorph assemblages from marine sediments due to the selective nature of sporomorph transport as a function of transport distance (Contreras et al., 2014; Moss et al., 2005). As such, even their occurrence in low numbers (e.g., ~1% of total sporomorph assemblage) can have substantial ecological significance and points toward the existence of peatlands and/or forested mires within the Site U1356 catchment area. The input of acidic peat into the marine realm is also consistent with the results of biome-based modeling suggesting that ~15%–20% of Antarctica was capable of supporting wetland and peat formation during the Eocene (DeConto et al., 2012).

4.2. Quantifying TerrOC Burial on the East Antarctic Margin During the EECO

Lipid biomarkers indicate that a considerable fraction of the OC pool on the early Eocene Wilkes Land continental margin is derived from the terrestrial biosphere. However, the relative proportion of terrestrial versus marine OC must be known in order to quantify TerrOC burial (Weijers et al., 2009). In modern settings, bulk OC $\delta^{13}C$ values ($\delta^{13}C_{org}$) can discriminate between marine OC (^{13}C-enriched) and vascular plant and/or soil OC (^{13}C-depleted). However, marine OC can be relatively ^{13}C-depleted during the Eocene (up to 7‰ relative to modern; Sluijs & Dickens, 2012) due to enhanced fractionation under higher CO_2 (Freeman & Hayes, 1992).

Here we use BIT indices (Hopmans et al., 2004) to characterize the fraction of terrestrial versus marine OC and employ a two end-member mixing-model:

$$f_{\text{terrestrial}} = (X_{\text{sample}} - X_{\text{marine}})/(X_{\text{terr}} - X_{\text{marine}}) * 100 \tag{4}$$

where $f_{\text{Terrestrial}}$ is the terrestrial OC fraction and X_{Sample} is the BIT index for the sediment sample (following Weijers et al., 2009). The marine- (X_{marine}) and terrestrial end-member (X_{terr}) for BIT is 0 and 0.91, respectively (Hopmans et al., 2004). The BIT index can reach a theoretical value of 1. However, BIT values in globally distributed soil samples average 0.91 (Weijers et al., 2006). Using our mixing-model approach, we estimate that the proportion of terrestrial OC in the Wilkes Land sediments ranges between 20% (minimum) and 65% (maximum). As the BIT index captures the proportion of soil OC (rather than soil and plant OC), this approach may underestimate the proportion of terrestrial OC in the Wilkes Land sediments. The BIT index has been shown to be controlled strongly by crenarchaeol—rather than brGDGT—concentrations, and may lead to a decoupling between BIT values and other terrestrial OC tracers (Smith et al., 2012). However, the fractional abundance of crenarchaeol is stable throughout the early Eocene (Bijl et al., 2013), arguing that BIT is largely controlled by changes in brGDGT abundance. The BIT index can also be influenced by in-situ marine or fluvial brGDGT production. However, brGDGTs reflect typical soil-distributions, with no abnormal Isomerization Ratio or #Rings$_{\text{tetra}}$ values (Sinninghe Damsté, 2016). This suggests negligible marine in situ or river production) and is consistent with other early Eocene sites in the southwest Pacific Ocean (e.g., Bijl et al., 2021).

The proportion of TerrOC can then be multiplied alongside TOC MARs to provide a first-order approximation of TerrOC sequestration along the Wilkes Land margin. This first requires an estimate of the Wilkes Land continental shelf area (118,675 km^2). Here we assume that the early Eocene shelf was similar to that of the latest Eocene (Paxman et al., 2019) and was significantly smaller than the present day continental shelf area (170,731 km^2). We also assume that the sediment package thickness (and thus, %TerrOC) is uniform. Assuming that 20%–65% of the OC pool in the Wilkes Land sediments is terrestrial-derived (see above), this implies the burial of 20–72 PgC of TerrOC the depositional interval (54.3 and 51.5 Ma). If we assume similar climate, vegetation distributions and transport mechanisms across the entire Antarctic shelf area (3,947,850 km^2), the potential mass of TerrOC sequestered is much larger (~410–1,300 PgC) and equates to a burial flux of 0.14–0.46 TgC/yr. These estimates are relatively modest compared to highly erosive mountainous river catchments (e.g., Taiwan; >8 TgC/yr; Kao et al., 2014) and large river systems (e.g., the Mackenzie River; 2.2 (+1.3/−0.9) TgC/yr; Hilton et al., 2015). To refine these estimates, additional studies at different localities are required. Additional seismic data may help to improve estimates of offshore sediment thickness, whilst the application of binary (or ternary) mixing models based on other geochemical proxies (e.g., C/N ratios, *n*-alkane/alkenone ratios) will help to refine our estimates of TerrOC burial (see Weijers et al., 2009). Until then, our estimates should be treated with caution.

Although these estimates incorporate various uncertainties, our work highlights the potential importance of continental margins as depocentres for TerrOC burial during the early Eocene. This is consistent with High Arctic continental shelf sediments deposited between the Palaeocene-Eocene Thermal Maximum (PETM; ~56 Ma)

and Eocene Thermal Maximum 2 (ETM2; ~53 Ma), which are dominated by long-chain n-alkyl lipids and low hydrogen indices (Boucsein & Stein, 2009; Weller & Stein, 2008). Terrigenous input–which is strongly correlated with TerrOC export in modern settings (e.g., Galy et al., 2015)–also increases during the EECO, including in New Zealand (e.g., Mead Stream; Nicolo et al., 2007; Slotnick et al., 2012) and the North Iberian margin (Payros et al., 2015). Enhanced TerrOC burial may be further promoted by larger, flatter drowned shelf areas during the Eocene (Bowen, 2013; Sømme et al., 2009). Taken together, this suggests an important role for continental shelves in storing terr(OC) during the Eocene. This is especially important given the evidence for low (terr)OC burial in open ocean Eocene environments (Olivarez Lyle & Lyle, 2006).

4.3. Hydroclimate Regulates TerrOC Export During Early Eocene

Enhanced TerrOC burial in coastal marine sediments could be driven by expansion of the terrestrial biosphere during the EECO. However, TerrOC export is largely controlled by precipitation (Hilton, 2017) and the capacity of rivers to erode and transport TerrOC (Galy et al., 2015). Here we explore whether hydroclimate regulates OC export from the terrestrial biosphere. To assess this, we use the hydrogen isotopic composition (δ^2H) of leaf wax (C_{27} and C_{29} n-alkane) biomarkers in a subset of samples deposited during the earliest Eocene (54.3–53.9 Ma) and EECO. C_{27} and C_{29} n-alkane δ^2H values average −190 and −195‰, respectively, and are comparable to those reported from other early Eocene-aged sites from similar latitudes (Speelman et al., 2010). The isotopic composition of precipitation (δ^2H$_w$) is estimated by assuming an apparent fractionation factor (^{2}H$\varepsilon_{wax/w}$) which integrates a range of variables (e.g., soil- and/or leaf water evapotranspiration, biosynthetic effects, vegetation type). Theoretical models have incorporated evaporative ^{2}H-enrichment of soil water into predictions of $^2\varepsilon_{wax/w}$ (Konecky et al., 2019; Smith & Freeman, 2006). However, in settings with extensive evaporation, woody plants take up rainwater opportunistically via different rooting strategies (Fan et al., 2017), resulting in minimal xylem water ^{2}H-enrichment. Although leaf water ^{2}H-enrichment is more variable (Daniels et al., 2017; Feakins et al., 2016; Kahmen et al., 2013), it is significantly reduced in warm and wet climates (Feakins et al., 2016). As the East Antarctic margin was characterized by elevated temperatures (>16° ± 5°C) and high precipitation (>1,300–1,600 mm/year; Pross et al., 2012), the impact of leaf water ^{2}H- enrichment is likely minimal.

Changes in the plant community can also influence the apparent fractionation between δ^2H$_{wax}$ and δ^2H$_w$ values. To account for the impact of vegetation isotope effects upon leaf wax δ^2H values, we developed a pollen-corrected fractionation factor (^{2}H$\varepsilon_{wax/w-corr}$) using a three endmember mixing model (following Feakins, 2013). This includes C_3 gymnosperms, C_3 dicots and pteridophytes (i.e., ferns) and is defined as:

$$^2H\varepsilon_{wax/w-corr} = f_{gymnosperm} * \varepsilon_{gymnosperm}] \ + \ [f_{dicot} * \varepsilon_{dicot}] \ + \ [f_{pteridophytes} * \varepsilon_{pteridophytes}] \tag{5}$$

where ε is based on the mean fractionation factor in modern plant types (Sachse et al., 2012) and f is based upon the percentage of pollen in adjacent samples (Contreras et al., 2013; Pross et al., 2012). Our pollen-corrected fractionation factor ranges between −107 and −113‰ and is higher than assumed in some Eocene studies (−130‰) (Handley et al., 2012; Pagani et al., 2006) but similar to an updated global data set of ^{2}H$\varepsilon_{wax/w}$ in modern systems (e.g., −121‰ for C_{29} n-alkane; McFarlin et al., 2019). When our pollen-corrected fractionation factor is applied to our leaf wax data set, we obtain δ^2H$_{w-corr}$ values which average −82‰ (C_{27} n-alkane; Figure 5b) and −83‰ (C_{29} n-alkane; Figure 5b). These values are ^{2}H-enriched relative to modern values (−99‰; based on iCESM1.2 pre-industrial x1 CO_2 simulation; see also below). There are several reasons for this. First, local air temperatures will yield more ^{2}H-enriched water vapor (a temperature effect) (Poulsen et al., 2007). Second, under warmer climates, decreased rainout efficiency at the low-latitudes (due to a reduction in vertical moisture transport) will result in more ^{2}H-enriched precipitation at the mid-to-high latitudes (e.g., Pagani et al., 2006). Our pollen-corrected δ^2H$_w$ values exhibit considerable variability in the earliest Eocene interval (ca. 30–40‰; Figure 5). This may represent changes in the hydroclimate regime. However, it could also record changes in OC source region. Indeed, sporomorph distributions indicate that TerrOC is derived from both the lowlands and higher-altitude hinterlands (Pross et al., 2012). Although leaf waxes typically provide a spatially integrated perspective, the spatial and temporal integration may vary by compound type and/or change through time. Future work using other compound classes (e.g., long-chain n-alkanoic acids) may help to differentiate between lowland (proximal) and highland (distal) OC sources (see Feakins et al., 2018; Hemingway et al., 2016).

Our pollen-corrected δ^2H$_w$ values indicate higher average δ^2H$_w$ values (e.g., −66‰ for the C_{29} n-alkane) during the EECO compared to the earliest Eocene (e.g., e.g., −90‰ for the C_{29} n-alkane; Figure 5b). This is consistent
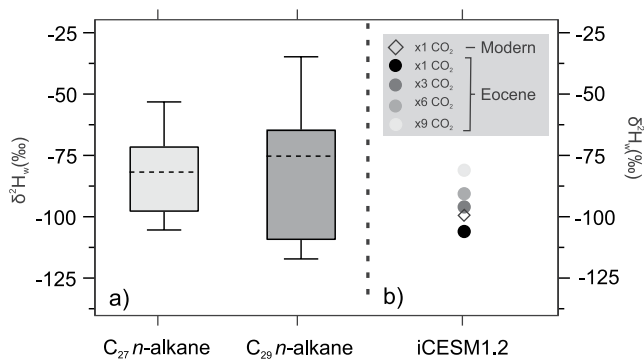
Figure 6. Reconstructed and simulated δ^2H_w on the East Antarctic margin during the early Eocene: (a) $\delta^2H_{w\text{-corr}}$ estimates inferred from the C_{27} n-alkane (light gray) and C_{29} n-alkane (dark gray). Dashed line represents median value. Box represents 1st and 3rd interquartile range. Whiskers represent 95% confidence interval. (b) model-derived δ^2H_w estimates inferred from iCESM1.2. Open triangle represents pre-industrial x1 CO_2 simulation. Closed circles represent Eocene simulations at four different CO_2 levels (x1, x3, x6, and x9 pre-industrial CO_2).

with an increase in poleward moisture transport in response to higher CO_2 and higher temperatures. To confirm that the higher average δ^2H_w values are due to higher CO_2 and/or higher temperatures, we calculate the precipitation-amount weighted δ^2H_w in isotope-enabled CESM simulations with a range of atmospheric CO2 concentrations (×1, ×3, ×6, and ×9 the preindustrial level; see Section 2.7). The modeled δ^2H_w exhibits a monotonic increase with the CO_2 concentrations in the simulations with values of $-106‰$ in ×1 CO_2, $-96‰$ in ×3 CO_2, $-91‰$ in ×6 CO_2 and $-81‰$ in ×9 CO_2 (Figure 6b). This δ^2H_w sensitivity to CO_2 levels in isotope-enabled climate models has been attributed to warmer temperatures and/or the associated reduction in isotopic rainout at low-latitudes (Poulsen et al., 2007; Speelman et al., 2010). The qualitatively consistent results between model simulations and proxy data supports our interpretation that the observed increase in proxy-inferred δ^2H_w values between the earliest Eocene and EECO ($\sim$20–40‰) is attributable to a CO_2-induced warming. There is also close data-model agreement in the absolute δ^2H_w values (Figure 6), supporting our data-based reconstructions. The impact from non-CO_2 boundary conditions on δ^2H_w can also be evaluated by comparing iCESM1.2 Eocene ×1 simulations against the pre-industrial simulation. This shows that the combined non-CO_2 boundary conditions (i.e., paleogeography, vegetation, aerosols, and removal of continental ice sheets) decrease δ^2H_w by $\sim$7‰. This implies that non-CO_2 boundary conditions exert a small secondary control on δ^2H_w values at our site. The iCESM1.2 simulations (x3, x6 and x9 PI CO_2 simulations) also exhibit high MAP estimates ($\sim$1310, 1520, and 1720 mm/year, respectively; Figures 7c and 7d) during the early Eocene. These are higher than previous simulations (Carmichael et al., 2016) but more consistent with existing sporomorph-based estimates (>1,300 mm/year [paratropical rainforest biome] and >1,600 mm/year [temperate rainforest biome]; Figures 7a and 7b; Pross et al., 2012). Slightly lower values (800–1,350 mm/year) have been reconstructed for Site U1356 based on climofunctions applied to detrital geochemistry (Passchier et al., 2013) and likely reflects the differences in the catchment sourcing.
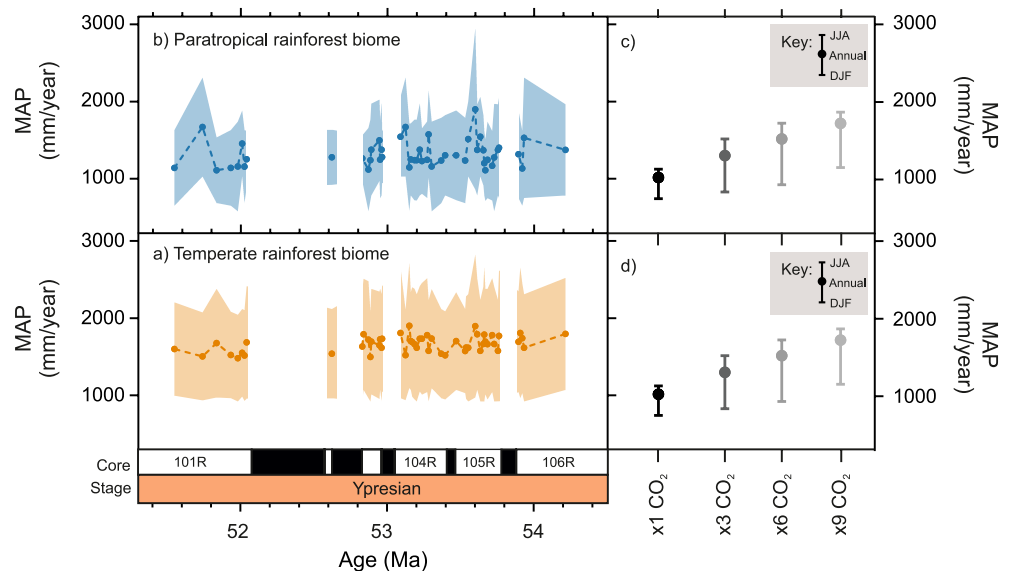

Figure 7. Long-term hydroclimate variability along the East Antarctic margin during the early Eocene. (a) mean annual precipitation (MAP) estimates for the temperate rainforest biome based on bioclimatic analysis (Pross et al., 2012), (b) MAP estimates for the paratropical rainforest biome based on bioclimatic analysis (Pross et al., 2012), (c) and (d) MAP estimates obtained via iCESM1.2 for four different CO_2 levels (x1, x3, x6, and x9 pre-industrial CO_2). Whiskers represent precipitation estimates during summer (JJA) and winter (DJF) months. Black segments indicate intervals of no core recovery.

Taken together, our results reveal that EECO was characterized by enhanced poleward moisture transport relative to the earliest Eocene (~54 Ma; Figures 5 and 6). The EECO also coincides with an interval of enhanced delivery of terrestrial OC into the marine realm (Figure 3), implying a causal link between the hydrological cycle and TerrOC burial at our site. Crucially, TerrOC burial can help to remove the atmospheric CO_2 and could serve as a negative feedback to decrease the surface temperature during intervals of global warmth. Compared to the silicate weathering feedback (which operates on the timescales of a million years), the organic carbon cycle operates over shorter timescales. As such, it could also be an important negative feedback during shorter-term warming events (e.g., hyperthermals).

5. Conclusions

The transport and burial of biospheric organic carbon in coastal marine sediments is an important carbon sink in modern settings. However, the relative importance of this feedback in past warm climates remains a major gap in our understanding. Using a multi-proxy approach, we find a significant increase in the accumulation rate of terrestrial biomarkers in early Eocene coastal marine sediments from offshore East Antarctica. As the early Eocene Antarctic continent was covered by a vast terrestrial OC reservoir ($>10^{15}$ PgC), the transport and subsequent burial of biospheric organic carbon in coastal marine sediments could have acted as a key CO_2 sink. This study highlights the importance of the terrestrial biosphere during past warm climates and its potential role as a negative feedback to stabilize Earth's surface temperature.

Conflict of Interest

The authors declare no conflicts of interest relevant to this study.

Data Availability Statement

The geochemical and numerical data used in the study are available at Pangaea (https://doi.pangaea.de/10.1594/PANGAEA.939793) and associated with a CC-BY 4.0 license.

References

Anagnostou, E., John, E. H., Babila, T. L., Sexton, P. F., Ridgwell, A., Lunt, D. J., et al. (2020). Proxy evidence for state-dependence of climate sensitivity in the Eocene greenhouse. *Nature Communications*, *11*(1), 1–9. https://doi.org/10.1038/s41467-020-17887-x

Berner, R. A. (1990). Atmospheric carbon dioxide levels over Phanerozoic time. *Science*, *249*, 1382–1386. https://doi.org/10.1126/science.249.4975.1382

Bijl, P. K., Bendle, J. A. P., Bohaty, S. M., Pross, J., Schouten, S., Tauxe, L., et al. (2013). Eocene cooling linked to early flow across the Tasmanian Gateway. *Proceedings of the National Academy of Sciences*, *110*, 9645–9650. https://doi.org/10.1073/pnas.1220872110

Bijl, P. K., Frieling, J., Cramwinckel, M. J., Boschman, C., Sluijs, A., & Peterse, F. (2021). Maastrichtian-Rupelian paleoclimates in the southwest Pacific–a critical evaluation of biomarker paleothermometry and dinoflagellate cyst paleoecology at Ocean Drilling Program Site 1172. *Climate of the Past Discussions*, *17*, 1–82.

Boucsein, B., & Stein, R. (2009). Black shale formation in the late Paleocene/early Eocene Arctic Ocean and paleoenvironmental conditions: New results from a detailed organic petrological study. *Marine and Petroleum Geology*, *26*, 416–426. https://doi.org/10.1016/j.marpetgeo.2008.04.001

Bowen, G. J. (2013). Up in smoke: A role for organic carbon feedbacks in Paleogene hyperthermals. *Global and Planetary Change*, *109*, 18–29. https://doi.org/10.1016/j.gloplacha.2013.07.001

Brady, E., Stevenson, S., Bailey, D., Liu, Z., Noone, D., Nusbaumer, J., et al. (2019). The connected isotopic water cycle in the Community Earth System Model version 1. *Journal of Advances in Modeling Earth Systems*, *11*, 2547–2566. https://doi.org/10.1029/2019ms001663

Bray, E. E., & Evans, E. D. (1961). Distribution of n-paraffins as a clue to recognition of source beds. *Geochimica et Cosmochimica Acta*, *22*, 2–15. https://doi.org/10.1016/0016-7037(61)90069-2

Carmichael, M. J., Lunt, D. J., Huber, M., Heinemann, M., Kiehl, J., LeGrande, A., et al. (2016). A model–model and data–model comparison for the early Eocene hydrological cycle. *Climate of the Past*, *12*, 455–481. https://doi.org/10.5194/cp-12-455-2016

Contreras, L., Pross, J., Bijl, P. K., Koutsodendris, A., Raine, J. I., van de Schootbrugge, B., & Brinkhuis, H. (2013). Early to middle Eocene vegetation dynamics at the Wilkes land margin (Antarctica). *Review of Palaeobotany and Palynology*, *197*, 119–142. https://doi.org/10.1016/j.revpalbo.2013.05.009

Contreras, L., Pross, J., Bijl, P. K., O'Hara, R. B., Raine, J. I., Sluijs, A., & Brinkhuis, H. (2014). Southern high-latitude terrestrial climate change during the Palaeocene–Eocene derived from a marine pollen record (ODP Site 1172, East Tasman Plateau). *Climate of the Past*, *10*, 1401–1420. https://doi.org/10.5194/cp-10-1401-2014

Dadey, K. A., Janecek, T., & Klaus, A. (1992). 37. Dry-bulk density: Its use and determination. *Proceedings of the Ocean Drilling Program, Scientific Results*, *126*.

Daniels, W. C., Russell, J. M., Giblin, A. E., Welker, J. M., Klein, E. S., & Huang, Y. (2017). Hydrogen isotope fractionation in leaf waxes in the Alaskan Arctic tundra. *Geochimica et Cosmochimica Acta*, *213*, 216–236. https://doi.org/10.1016/j.gca.2017.06.028

DeConto, R. M., Galeotti, S., Pagani, M., Tracy, D., Schaefer, K., Zhang, T., et al. (2012). Past extreme warming events linked to massive carbon release from thawing permafrost. *Nature*, *484*, 87–91. https://doi.org/10.1038/nature10929

Diefendorf, A. F., & Freimuth, E. J. (2017). Extracting the most from terrestrial plant-derived n-alkyl lipids and their carbon isotopes from the sedimentary record: A review. *Organic Geochemistry*, *103*, 1–21. https://doi.org/10.1016/j.orggeochem.2016.10.016

Eglinton, G., & Hamilton, R. J. (1967). Leaf epicuticular waxes. *Science*, *156*, 1322–1335. https://doi.org/10.1126/science.156.3780.1322

Eglinton, T. I., Galy, V. V., Hemingway, J. D., Feng, X., Bao, H., Blattmann, T. M., et al. (2021). Climate control on terrestrial biospheric carbon turnover. *Proceedings of the National Academy of Sciences*, *118*. https://doi.org/10.1073/pnas.2011585118

Escutia, C., Brinkhuis, H., & Klaus, A. (2011). *Proceedings of the Integrated Ocean Drilling Program* (Vol. 318). Integrated Ocean Drilling Program Management International, Inc.

Escutia, C., Brinkhuis, H., Klaus, A., & the IODP Expedition 318 Scientists (2011). IODP Expedition 318; from greenhouse to icehouse at the Wilkes land Antarctic margin. *Scientific Drilling*, *12*, 15–23. https://doi.org/10.5194/sd-12-15-2011

Fan, Y., Miguez-Macho, G., Jobbágy, E. G., Jackson, R. B., & Otero-Casal, C. (2017). Hydrologic regulation of plant rooting depth. *Proceedings of the National Academy of Sciences*, *114*, 10572–10577. https://doi.org/10.1073/pnas.1712381114

Feakins, S. J. (2013). Pollen-corrected leaf wax D/H reconstructions of northeast African hydrological changes during the late Miocene. *Palaeogeography, Palaeoclimatology, Palaeoecology*, *374*, 62–71. https://doi.org/10.1016/j.palaeo.2013.01.004

Feakins, S. J., Bentley, L. P., Salinas, N., Shenkin, A., Blonder, B., Goldsmith, G. R., et al. (2016). Plant leaf wax biomarkers capture gradients in hydrogen isotopes of precipitation from the Andes and Amazon. *Geochimica et Cosmochimica Acta*, *182*, 155–172. https://doi.org/10.1016/j.gca.2016.03.018

Feakins, S. J., Wu, M. S., Ponton, C., Galy, V., & West, A. J. (2018). Dual isotope evidence for sedimentary integration of plant wax biomarkers across an Andes-Amazon elevation transect. *Geochimica et Cosmochimica Acta*, *242*, 64–81. https://doi.org/10.1016/j.gca.2018.09.007

Francis, J. E., & Poole, I. (2002). Cretaceous and early Tertiary climates of Antarctica: Evidence from fossil wood. *Palaeogeography, Palaeoclimatology, Palaeoecology*, *182*(1–2), 47–64. https://doi.org/10.1016/s0031-0182(01)00452-7

Freeman, K. H., & Hayes, J. (1992). Fractionation of carbon isotopes by phytoplankton and estimates of ancient CO_2 levels. *Global Biogeochemical Cycles*, *6*, 185–198. https://doi.org/10.1029/92gb00190

Fretwell, P., Pritchard, H. D., Vaughan, D. G., Bamber, J. L., Barrand, N. E., Bell, R., et al. (2013). Bedmap2: Improved ice bed, surface and thickness datasets for Antarctica. *The Cryosphere*, *7*, 375–393. https://doi.org/10.5194/tc-7-375-2013

Gaillardet, J., Dupré, B., Louvat, P., & Allegre, C. J. (1999). Global silicate weathering and CO_2 consumption rates deduced from the chemistry of large rivers. *Chemical Geology*, *159*(1–4), 3–30. https://doi.org/10.1016/s0009-2541(99)00031-5

Galy, V., France-Lanord, C., Beyssac, O., Faure, P., Kudrass, H., & Palhol, F. (2007). Efficient organic carbon burial in the Bengal fan sustained by the Himalayan erosional system. *Nature*, *450*(7168), 407–410. https://doi.org/10.1038/nature06273

Galy, V., Peucker-Ehrenbrink, B., & Eglinton, T. (2015). Global carbon export from the terrestrial biosphere controlled by erosion. *Nature*, *521*, 204–207. https://doi.org/10.1038/nature14400

Guo, L., Semiletov, I., Gustafsson, Ö., Ingri, J., Andersson, P., Dudarev, O., & White, D. (2004). Characterization of Siberian Arctic coastal sediments: Implications for terrestrial organic carbon export. *Global Biogeochemical Cycles*, *18*(1). https://doi.org/10.1029/2003gb002087

Handley, L., O'Halloran, A., Pearson, P. N., Hawkins, E., Nicholas, C. J., Schouten, S., et al. (2012). Changes in the hydrological cycle in tropical East Africa during the Paleocene–Eocene thermal maximum. *Palaeogeography, Palaeoclimatology, Palaeoecology*, *329*, 10–21. https://doi.org/10.1016/j.palaeo.2012.02.002

Hayes, J. (1993). Factors controlling 13C contents of sedimentary organic compounds: Principles and evidence. *Marine Geology*, *113*, 111–125. https://doi.org/10.1016/0025-3227(93)90153-m

Hemingway, J. D., Schefuß, E., Dinga, B. J., Pryer, H., & Galy, V. V. (2016). Multiple plant-wax compounds record differential sources and ecosystem structure in large river catchments. *Geochimica et Cosmochimica Acta*, *184*, 20–40. https://doi.org/10.1016/j.gca.2016.04.003

Herold, N., Buzan, J., Seton, M., Goldner, A., Green, J., Müller, R. D., et al. (2014). A suite of early Eocene (~55 Ma) climate model boundary conditions. *Geoscientific Model Development*, *7*(5), 2077–2090.

Hilton, R. G. (2017). Climate regulates the erosional carbon export from the terrestrial biosphere. *Geomorphology*, *277*, 118–132. https://doi.org/10.1016/j.geomorph.2016.03.028

Hilton, R. G., Gaillardet, J., Calmels, D., & Birck, J. L. (2014). Geological respiration of a mountain belt revealed by the trace element rhenium. *Earth and Planetary Science Letters*, *403*, 27–36. https://doi.org/10.1016/j.epsl.2014.06.021

Hilton, R. G., Galy, V., Gaillardet, J., Dellinger, M., Bryant, C., O'Regan, M., et al. (2015). Erosion of organic carbon in the Arctic as a geological carbon dioxide sink. *Nature*, *524*, 84–87. https://doi.org/10.1038/nature14653

Hilton, R. G., & West, A. J. (2020). Mountains, erosion and the carbon cycle. *Nature Reviews Earth & Environment*, *1*, 284–299. https://doi.org/10.1038/s43017-020-0058-6

Hochmuth, K., Gohl, K., Leitchenkov, G., Sauermilch, I., Whittaker, J. M., Uenzelmann-Neben, G., et al. (2020). The evolving paleobathymetry of the circum-Antarctic Southern Ocean since 34 Ma: A key to understanding past cryosphere-ocean developments. *Geochemistry, Geophysics, Geosystems*, *21*, e2020GC009122. https://doi.org/10.1029/2020gc009122

Hochmuth, K., Paxman, G., Jamieson, S. S., Gohl, K., Leitchenkov, G., Bentley, M. J., et al. (2020). *Combined palaeotopography and palaeobathymetry of the Antarctic continent and the Southern Ocean since 34 Ma*. PANGAEA. https://doi.pangaea.de/10.1594/PANGAEA.923109

Hollis, C. J., Dunkley Jones, T., Anagnostou, E., Bijl, P. K., Cramwinckel, M. J., Cui, Y., et al. (2019). The DeepMIP contribution to PMIP4: Methodologies for selection, compilation and analysis of latest Paleocene and early Eocene climate proxy data, incorporating version 0.1 of the DeepMIP database. *Geoscientific Model Development*, *12*, 3149–3206. https://doi.org/10.5194/gmd-12-3149-2019

Hopmans, E. C., Weijers, J. W., Schefuß, E., Herfort, L., Sinninghe Damsté, J. S., & Schouten, S. (2004). A novel proxy for terrestrial organic matter in sediments based on branched and isoprenoid tetraether lipids. *Earth and Planetary Science Letters*, *224*, 107–116. https://doi.org/10.1016/j.epsl.2004.05.012

Inglis, G. N., Bragg, F., Burls, N. J., Cramwinckel, M. J., Evans, D., Foster, G. L., et al. (2020). Global mean surface temperature and climate sensitivity of the early Eocene climatic Optimum (EECO), Paleocene–Eocene thermal maximum (PETM), and latest Paleocene. *Climate of the Past*, *16*, 1953–1968. https://doi.org/10.5194/cp-16-1953-2020

Inglis, G. N., Collinson, M. E., Riegel, W., Wilde, V., Robson, B. E., Lenz, O. K., & Pancost, R. D. (2015). Ecological and biogeochemical change in an early Paleogene peat-forming environment: Linking biomarkers and palynology. *Palaeogeography, Palaeoclimatology, Palaeoecology*, *438*, 245–255. https://doi.org/10.1016/j.palaeo.2015.08.001

Inglis, G. N., Naafs, B. D. A., Zheng, Y., McClymont, E. L., Evershed, R. P., & Pancost, R. D. (2018). Distributions of geohopanoids in peat: Implications for the use of hopanoid-based proxies in natural archives. *Geochimica et Cosmochimica Acta*, *224*, 249–261. https://doi.org/10.1016/j.gca.2017.12.029

Inglis, G. N., Naafs, B. D. A., Zheng, Y., Schellekens, J., & Pancost, R. D. (2019). δ13C values of bacterial hopanoids and leaf waxes as tracers for methanotrophy in peatlands. *Geochimica et Cosmochimica Acta*, *260*, 244–256. https://doi.org/10.1016/j.gca.2019.06.030

Kahmen, A., Hoffmann, B., Schefuß, E., Arndt, S. K., Cernusak, L. A., West, J. B., & Sachse, D. (2013). Leaf water deuterium enrichment shapes leaf wax n-alkane δD values of angiosperm plants II: Observational evidence and global implications. *Geochimica et Cosmochimica Acta*, *111*, 50–63. https://doi.org/10.1016/j.gca.2012.09.004

Kao, S.-J., Hilton, R., Selvaraj, K., Dai, M., Zehetner, F., Huang, J.-C., et al. (2014). Preservation of terrestrial organic carbon in marine sediments offshore Taiwan: Mountain building and atmospheric carbon dioxide sequestration. *Earth Surface Dynamics*, *2*, 127–139. https://doi.org/10.5194/esurf-2-127-2014

Konecky, B., Noone, D., & Cobb, K. (2019). The influence of competing hydroclimate processes on stable isotope ratios in tropical rainfall. *Geophysical Research Letters*, *46*, 1622–1633. https://doi.org/10.1029/2018gl080188

Lee, J. E., Fung, I., DePaolo, D. J., & Henning, C. C. (2007). Analysis of the global distribution of water isotopes using the NCAR atmospheric general circulation model. *Journal of Geophysical Research*, *112*(D16). https://doi.org/10.1029/2006jd007657

Lunt, D. J., Bragg, F., Chan, W.-L., Hutchinson, D. K., Ladant, J.-B., Morozova, P., et al. (2021). DeepMIP: Model intercomparison of early Eocene climatic optimum (EECO) large-scale climate features and comparison with proxy data. *Climate of the Past*, *17*, 203–227. https://doi.org/10.5194/cp-17-203-2021

Lunt, D. J., Huber, M., Anagnostou, E., Baatsen, M. L., Caballero, R., DeConto, R., et al. (2017). The DeepMIP contribution to PMIP4: Experimental design for model simulations of the EECO, PETM, and pre-PETM (version 1.0). *Geoscientific Model Development*, *10*, 889–901. https://doi.org/10.5194/gmd-10-889-2017

Mackenzie, A., Patience, R., Maxwell, J., Vandenbroucke, M., & Durand, B. (1980). Molecular parameters of maturation in the Toarcian shales, Paris Basin, France—I. Changes in the configurations of acyclic isoprenoid alkanes, steranes and triterpanes. *Geochimica et Cosmochimica Acta*, *44*, 1709–1721. https://doi.org/10.1016/0016-7037(80)90222-7

McFarlin, J. M., Axford, Y., Masterson, A. L., & Osburn, M. R. (2019). Calibration of modern sedimentary δ2H plant wax-water relationships in Greenland lakes. *Quaternary Science Reviews*, *225*, 105978. https://doi.org/10.1016/j.quascirev.2019.105978

Moss, P. T., Kershaw, A. P., & Grindrod, J. (2005). Pollen transport and deposition in riverine and marine environments within the humid tropics of northeastern Australia. *Review of Palaeobotany and Palynology*, *134*, 55–69. https://doi.org/10.1016/j.revpalbo.2004.11.003

Nicolo, M. J., Dickens, G. R., Hollis, C. J., & Zachos, J. C. (2007). Multiple early Eocene hyperthermals: Their sedimentary expression on the New Zealand continental margin and in the deep sea. *Geology*, *35*, 699–702. https://doi.org/10.1130/g23648a.1

Olivarez Lyle, A., & Lyle, M. W. (2006). Missing organic carbon in Eocene marine sediments: Is metabolism the biological feedback that maintains end-member climates? *Paleoceanography*, *21*. https://doi.org/10.1029/2005pa001230

Pagani, M., Pedentchouk, N., Huber, M., Sluijs, A., Schouten, S., Schouten, S., et al. (2006). Arctic hydrology during global warming at the Palaeocene/Eocene thermal maximum. *Nature*, *442*, 671–675. https://doi.org/10.1038/nature05043

Pancost, R. D., & Boot, C. S. (2004). The palaeoclimatic utility of terrestrial biomarkers in marine sediments. *Marine Chemistry*, *92*, 239–261. https://doi.org/10.1016/j.marchem.2004.06.029

Passchier, S., Bohaty, S. M., Jiménez-Espejo, F., Pross, J., Röhl, U., van de Flierdt, T., et al. (2013). Early Eocene to middle Miocene cooling and aridification of East Antarctica. *Geochemistry, Geophysics, Geosystems*, *14*, 1399–1410. https://doi.org/10.1002/ggge.20106

Paxman, G. J., Jamieson, S. S., Hochmuth, K., Gohl, K., Bentley, M. J., Leitchenkov, G., & Ferraccioli, F. (2019). Reconstructions of Antarctic topography since the Eocene–Oligocene boundary. *Palaeogeography, Palaeoclimatology, Palaeoecology*, *535*, 109346. https://doi.org/10.1016/j.palaeo.2019.109346

Payros, A., Ortiz, S., Millán, I., Arostegi, J., Orue-Etxebarria, X., & Apellaniz, E. (2015). Early Eocene climatic optimum: Environmental impact on the North Iberian continental margin. *Bulletin*, *127*, 1632–1644. https://doi.org/10.1130/b31278.1

Plank, T., & Manning, C. E. (2019). Subducting carbon. *Nature*, *574*(7778), 343–352. https://doi.org/10.1038/s41586-019-1643-z

Polissar, P. J., & D'Andrea, W. J. (2014). Uncertainty in paleohydrologic reconstructions from molecular δD values. *Geochimica et Cosmochimica Acta*, *129*, 146–156. https://doi.org/10.1016/j.gca.2013.12.021

Poulsen, C. J., Pollard, D., & White, T. S. (2007). General circulation model simulation of the δ18O content of continental precipitation in the middle Cretaceous: A model-proxy comparison. *Geology*, *35*, 199–202. https://doi.org/10.1130/g23343a.1

Pross, J., Contreras, L., Bijl, P. K., Greenwood, D. R., Bohaty, S. M., Bohaty, S. M., et al. (2012). Persistent near-tropical warmth on the Antarctic continent during the early Eocene epoch. *Nature*, *488*, 73–77. https://doi.org/10.1038/nature11300

Sachse, D., Billault, I., Bowen, G. J., Chikaraishi, Y., Dawson, T. E., Feakins, S. J., et al. (2012). Molecular paleohydrology: Interpreting the hydrogen-isotopic composition of lipid biomarkers from photosynthesizing organisms. *Annual Review of Earth and Planetary Sciences*, *40*, 221–249. https://doi.org/10.1146/annurev-earth-042711-105535

Schmidt, G. A., LeGrande, A. N., & Hoffmann, G. (2007). Water isotope expressions of intrinsic and forced variability in a coupled ocean-atmosphere model. *Journal of Geophysical Research*, *112*(D10). https://doi.org/10.1029/2006jd007781

Semiletov, I. P., Pipko, I. I., Shakhova, N. E., Dudarev, O. V., Pugach, S. P., Charkin, A. N., et al. (2011). Carbon transport by the Lena River from its headwaters to the Arctic Ocean, with emphasis on fluvial input of terrestrial particulate organic carbon vs. carbon transport by coastal erosion. *Biogeosciences*, *8*(9), 2407–2426. https://doi.org/10.5194/bg-8-2407-2011

Sessions, A. L., Burgoyne, T. W., Schimmelmann, A., & Hayes, J. M. (1999). Fractionation of hydrogen isotopes in lipid biosynthesis. *Organic Geochemistry*, *30*, 1193–1200. https://doi.org/10.1016/s0146-6380(99)00094-7

Sinninghe Damsté, J. S. (2016). Spatial heterogeneity of sources of branched tetraethers in shelf systems: The geochemistry of tetraethers in the Berau River delta (Kalimantan, Indonesia). *Geochimica et Cosmochimica Acta*, *186*, 13–31. https://doi.org/10.1016/j.gca.2016.04.033

Slotnick, B. S., Dickens, G. R., Nicolo, M. J., Hollis, C. J., Crampton, J. S., Zachos, J. C., & Sluijs, A. (2012). Large-amplitude variations in carbon cycling and terrestrial weathering during the latest Paleocene and earliest Eocene: The record at Mead Stream, New Zealand. *The Journal of Geology*, *120*, 487–505. https://doi.org/10.1086/666743

Sluijs, A., & Dickens, G. R. (2012). Assessing offsets between the δ13C of sedimentary components and the global exogenic carbon pool across early Paleogene carbon cycle perturbations. *Global Biogeochemical Cycles*, *26*. https://doi.org/10.1029/2011gb004224

Smith, F. A., & Freeman, K. H. (2006). Influence of physiology and climate on δD of leaf wax n-alkanes from C3 and C4 grasses. *Geochimica et Cosmochimica Acta*, *70*, 1172–1187. https://doi.org/10.1016/j.gca.2005.11.006

Smith, R. W., Bianchi, T. S., & Li, X. (2012). A re-evaluation of the use of branched GDGTs as terrestrial biomarkers: Implications for the BIT Index. *Geochimica et Cosmochimica Acta*, *80*, 14–29. https://doi.org/10.1016/j.gca.2011.11.025

Smittenberg, R., Pancost, R., Hopmans, E., Paetzel, M., & Damsté, J. S. (2004). A 400-year record of environmental change in an euxinic fjord as revealed by the sedimentary biomarker record. *Palaeogeography, Palaeoclimatology, Palaeoecology*, *202*, 331–351. https://doi.org/10.1016/s0031-0182(03)00642-4

Sømme, T. O., Helland-Hansen, W., & Granjeon, D. (2009). Impact of eustatic amplitude variations on shelf morphology, sediment dispersal, and sequence stratigraphic interpretation: Icehouse versus greenhouse systems. *Geology*, *37*, 587–590.

Sparkes, R. B., Doğrul Selver, A., Bischoff, J., Talbot, H. M., Gustafsson, Ö., Semiletov, I. P., et al. (2015). GDGT distributions on the East Siberian Arctic shelf: Implications for organic carbon export, burial and degradation. *Biogeosciences*, *12*, 3753–3768. https://doi.org/10.5194/bg-12-3753-2015

Speelman, E. N., Sewall, J. O., Noone, D., Huber, M., der Heydt, A., Damsté, J. S., & Reichart, G.-J. (2010). Modeling the influence of a reduced equator-to-pole sea surface temperature gradient on the distribution of water isotopes in the Early/Middle Eocene. *Earth and Planetary Science Letters*, *298*, 57–65. https://doi.org/10.1016/j.epsl.2010.07.026

Talbot, H. M., & Farrimond, P. (2007). Bacterial populations recorded in diverse sedimentary biohopanoid distributions. *Organic Geochemistry*, *38*, 1212–1225. https://doi.org/10.1016/j.orggeochem.2007.04.006

Tauxe, L., Stickley, C. E., Sugisaki, S., Bijl, P. K., Bohaty, S. M., Brinkhuis, H., et al. (2012). Chronostratigraphic framework for the IODP Expedition 318 cores from the Wilkes Land margin; constraints for paleoceanographic reconstruction. *Paleoceanography*, *27*. https://doi.org/10.1029/2012pa002308

Torres, M. A., West, A. J., & Li, G. (2014). Sulphide oxidation and carbonate dissolution as a source of CO_2 over geological timescales. *Nature*, *507*(7492), 346–349. https://doi.org/10.1038/nature13030

Wang, J., Howarth, J. D., McClymont, E. L., Densmore, A. L., Fitzsimons, S. J., Croissant, T., et al. (2020). Long-term patterns of hillslope erosion by earthquake-induced landslides shape mountain landscapes. *Science Advances*, *6*(23), eaaz6446. https://doi.org/10.1126/sciadv.aaz6446

Weijers, J. W., Schouten, S., Schefuß, E., Schneider, R. R., & Damste, J. S. S. (2009). Disentangling marine, soil and plant organic carbon contributions to continental margin sediments: A multi-proxy approach in a 20,000 year sediment record from the Congo deep-sea fan. *Geochimica et Cosmochimica Acta*, *73*, 119–132. https://doi.org/10.1016/j.gca.2008.10.016

Weijers, J. W., Schouten, S., Spaargaren, O. C., & Damsté, J. S. S. (2006). Occurrence and distribution of tetraether membrane lipids in soils: Implications for the use of the TEX86 proxy and the BIT index. *Organic Geochemistry*, *37*, 1680–1693. https://doi.org/10.1016/j.orggeochem.2006.07.018

Weller, P., & Stein, R. (2008). Paleogene biomarker records from the central Arctic Ocean (Integrated Ocean Drilling Program Expedition 302): Organic carbon sources, anoxia, and sea surface temperature. *Paleoceanography*, *23*. https://doi.org/10.1029/2007pa001472

Zhu, J., Poulsen, C. J., Otto-Bliesner, B. L., Liu, Z., Brady, E. C., & Noone, D. C. (2020). Simulation of early Eocene water isotopes using an Earth system model and its implication for past climate reconstruction. *Earth and Planetary Science Letters*, *537*, 116164. https://doi.org/10.1016/j.epsl.2020.116164

Zhu, J., Poulsen, C. J., & Tierney, J. E. (2019). Simulation of Eocene extreme warmth and high climate sensitivity through cloud feedbacks. *Science Advances*, *5*, eaax1874. https://doi.org/10.1126/sciadv.aax1874